Electric field strengths within a micro cavity plasma array measured by Stark shift and splitting of a helium line pair

Sebastian Dzikowski, David Steuer, Sylvain Iséni, Judith Golda, Marc Böke, Volker Schulz-von der Gathen

▶ **To cite this version:**

Sebastian Dzikowski, David Steuer, Sylvain Iséni, Judith Golda, Marc Böke, et al.. Electric field strengths within a micro cavity plasma array measured by Stark shift and splitting of a helium line pair. Plasma Sources Science and Technology, 2022, 31 (6), pp.065014. 10.1088/1361-6595/ac7820 . hal-03721709

HAL Id: hal-03721709
https://hal.science/hal-03721709v1

Submitted on 12 Jul 2022

HAL is a multi-disciplinary open access archive for the deposit and dissemination of scientific research documents, whether they are published or not. The documents may come from teaching and research institutions in France or abroad, or from public or private research centers.

L'archive ouverte pluridisciplinaire **HAL**, est destinée au dépôt et à la diffusion de documents scientifiques de niveau recherche, publiés ou non, émanant des établissements d'enseignement et de recherche français ou étrangers, des laboratoires publics ou privés.

Distributed under a Creative Commons Attribution 4.0 International License

OPEN ACCESS
IOP Publishing
Plasma Sources Science and Technology
Plasma Sources Sci. Technol. **31** (2022) 065014 (15pp)
https://doi.org/10.1088/1361-6595/ac7820

Electric field strengths within a micro cavity plasma array measured by Stark shift and splitting of a helium line pair

Sebastian Dzikowski[1,*], David Steuer[3], Sylvain Iséni[2], Judith Golda[3], Marc Böke[1] and Volker Schulz-von der Gathen[1]

[1] Experimental Physics II, Ruhr-University Bochum, Universitätsstr. 150, 44801 Bochum, Germany
[2] GREMI–Groupe de Recherches sur l'Énergétique des Milieux Ionisés—UMR 7344, CNRS/Université d'Orléans, France
[3] Plasma Interface Physics, Ruhr-University Bochum, Universitätsstr. 150, 44801 Bochum, Germany

E-mail: sebastian.dzikowski@rub.de

Received 2 February 2022, revised 26 May 2022
Accepted for publication 13 June 2022
Published 5 July 2022

Abstract

The electric field is a fundamental parameter for plasma sources and devices. Its knowledge is a dominant setscrew for many processes such as controllable fluxes and energies of charged particles onto surfaces and for the electron energy distribution function. However, experimental data of electric field strengths in micro-structured surface dielectric barrier discharges are rare. Due to geometric configurations and dimensions in micrometer scale, probe-based investigations are challenging. To tackle these issues, we exploit the optical access into micro cavities of a plasma array operated with pure helium to use the Stark effect of the allowed 492.19 nm ($^1D \mapsto {}^1P^0$) and forbidden 492.06 nm helium line ($^1F^0 \mapsto {}^1P^0$). Based on it, we present spatially-integrated and time-resolved electric field strengths in a range between 20 kV cm^{-1} and 60 kV cm^{-1} depending on various parameters such as cavity diameters in 100 μm range and excitation properties. The obtained electric fields can be controlled just by bipolarity of applied voltage and show a good agreement to previous simulated field strengths in pore and silicon-based devices. As expected from simulation dealing with discharges in pores, a smaller cavity dimension yields higher electric field strengths. Due to these high electric fields and the option of this plasma source to easily integrate a catalyst in the discharge volume, this micro cavity plasma array promises further insights into plasma-enhanced catalysis.

Keywords: atmospheric pressure plasma, microplasma, dielectric barrier discharge, micro cavity plasma array, optical emission spectroscopy, Stark shifting and splitting, plasma catalysis

(Some figures may appear in colour only in the online journal)

* Author to whom any correspondence should be addressed.

Original content from this work may be used under the terms of the Creative Commons Attribution 4.0 licence. Any further distribution of this work must maintain attribution to the author(s) and the title of the work, journal citation and DOI.

 © 2022 The Author(s). Published by IOP Publishing Ltd

1. Introduction

Micro-structured plasma discharges operating at or near atmospheric pressure are regarded to have a vast potential for technical applications [1]. Among others [2, 3] plasma catalysis is one of the most interesting possible fields of application [4, 5]. Plasma catalysis can be realised in two different configurations: (1) plasma and catalyst are in direct contact in the so-called single-stage or in-plasma catalysis. Due to this direct interaction, properties of the plasma and the catalyst such as the electric field or the morphology can influence one another. (2) In a two-stage or post-plasma catalysis the plasma is spatially separated and only the reformed gas flow interacts with the catalyst [6].

One of the most fundamental plasma parameters is the microscopic electric field strength [7, 8]. In the case that the electric field is controllable by operation parameters in space and time, charged particle fluxes and energies on surfaces can be controlled [7, 9]. Thus, laboratory plasmas can be optimised with respect to their applications and understanding and modelling approaches are supported. Of particular importance is the electric field with regard to plasma-enhanced catalysis in dielectric barrier discharges (DBD) having an engraved micro-dimensional pore in one of the dielectrics covering the electrodes [10]. Zhang *et al* showed in a simulation approach that the electric field is clearly increased inside this pore in comparison to the discharge volume between the electrodes yielding higher electron densities and ionisation rates. This subsequently affects plasma catalytic processes [10].

A candidate for comparable experiments is realised by so-called micro cavity plasma arrays (MCPA) [1, 11–13]. One representative is a modular and flexible layer-constructed metal grid array (MGA) consisting of two electrodes separated by a dielectric foil. The high voltage supplied electrode contains hundreds to thousands of regularly arranged cavities in the 100 μm range [13]. The confinement into the cavities is the main characteristic of the array devices and ensures a reproducible and defined operation. Despite this special setup, these arrays show general features of surface DBDs and promise high electric fields within the individual cavities. Furthermore, this plasma source offers the opportunity to integrate a catalyst on dielectric for investigating the plasma–catalyst interaction [13].

However, experimental data on electric fields in micro-discharges with dielectric barriers are rather limited [14–16]. Due to the micrometer scale and structure of such devices, electric probes are not suitable contrary to filamentary DBDs [17]. Similarly, optical access for laser-based methods is often prevented [18]. Therefore, often emission-based techniques are applied. One way to measure electric field strengths is based on the relative line intensity ratio of nitrogen such as the 'second positive system' (N_2(C-B, 0-0)) and 'first negative system' (N_2^+(B-X, 0-0)) [8, 19]. However, a disadvantage of this method is that depending on the operating gas, a certain amount of nitrogen might have to be admixed in order to detect a sufficient signal from the named nitrogen systems. This in consequence might affect the discharge characteristics too much. Furthermore, these methods and corresponding models require the knowledge of other plasma parameters such as the EEDF.

The unobstructed optical access of the MGA allows to exploit the Stark effect which causes a splitting and shifting of atomic spectral lines in presence of strong electric field strengths. This optical approach was already successfully applied on different discharges [7, 20–23]. The proportionate correlation between the displacement of these transitions and the occurring electric field was theoretically approximated based on quantum mechanical perturbation principles by Foster [24]. This *ab initio* method [7] does not require the knowledge of further plasma parameters.

This paper presents time-resolved and spatially-integrated measurements of the electric field strengths in a MGA surface DBD operated in pure helium with time resolutions up to 1 μs. Here, to resolve and to measure the spectral components a plane grating spectrometer backed with an iCCD-camera is used. The surface DBD [13] is supplied with a bipolar triangular waveform excitation and allows a simultaneous operation of four arrays with different cavity diameters in the 100 μm range comparable to experiments on silicon-based micro arrays [25]. To obtain a better understanding, the electric field is investigated half-phase resolved in dependency on typical excitation and operation parameters such as the applied voltage amplitude, frequency and pressure. For these investigations, the displacement between the allowed 492.19 nm ($^1D \mapsto {}^1P^0$) helium transition and the forbidden 492.06 nm ($^1D \mapsto {}^1F^0$) counterpart is resolved. A simple Townsend model is set up to understand the influence of bipolar excitation and operation parameters on electric field strengths within the cavities.

2. Stark effect

In this work, we use the linear Stark effect in helium to measure macroscopic electric field strengths within a MGA. The strong interaction with the occurring electric field causes a splitting and shifting of atomic sub-levels and consequently a partial resolution of the degeneracy of these levels. As a result, optical transitions between an upper state $\Psi_\mathrm{u}(n_\mathrm{u}, l_\mathrm{u}, m_\mathrm{u})$ and a lower state $\Psi_\mathrm{l}(n_\mathrm{l}, l_\mathrm{l}, m_\mathrm{l})$, denominated by the principal quantum number n, the angular quantum number l and the magnetic quantum number m, also exhibit line shifting and splitting. For optically allowed dipole transitions the following selection rules apply:

$$\Delta l = l_\mathrm{u} - l_\mathrm{l} = \pm 1, \tag{1}$$

$$\Delta m = m_\mathrm{u} - m_\mathrm{l} = 0, \pm 1. \tag{2}$$

For hydrogen, the linear Stark effect can be described analytically since the time-dependent Schrödinger equation can be solved completely. In the case of helium, the situation is more complex due to the additional second electron. The Coulomb interaction between these two electrons results in a not analytically solvable time-dependent Schrödinger equation.

However, a theoretical approximation for higher principal quantum numbers in helium was provided by Foster [24].

By using a quantum mechanical perturbation principle it is possible to determine the energetic displacements for the upper levels with $n_u = 4$ or 5 depending on the electric field strengths. This theoretical approximation for helium is based on a hydrogen-like potential and explained in detail in [20, 24].

In the case of helium, optically forbidden quadrupole transitions can be observed under the influence of strong electric fields. This allows to measure the electric field based on the so-called 'allowed-forbidden method' which depends on shifting and splitting between optical allowed and optical forbidden transitions and its intensities. Since the intensity ratios show a low sensitivity for electric field strengths of about 20 kV cm^{-1} [26, 27], this work is just dealing with wavelength displacements. Here, the selection rule changes with respect to the angular quantum number are

$$\Delta l = l_u - l_l = \pm 2. \tag{3}$$

The chosen transitions to observe the shifting and splitting are the allowed 492.19 nm ($^1D \mapsto {}^1P^0$, $\Delta l = -1$) and forbidden 492.06 nm ($^1F^0 \mapsto {}^1P^0$, $\Delta l = -2$) ones, each consisting of several sub-transitions. This pair is selected as a compromise of strong splitting, the simplicity of the evolving spectra and high intensities of forbidden sub-transitions over other candidates as discussed by Cvetanovic *et al* [7]. Additionally, it fits best the spectral sensitivity of our optical system and showed no interference with other emission lines. As a result of the interaction with the electric field, allowed sub-transitions shift to larger wavelengths with increasing electric field strengths complying with selection rules 1 and 2, while forbidden sub-transitions move in the opposite direction following selection rules 2 and 3. The resulting displacements between forbidden and allowed sub-transitions can then be transferred into electric field strengths by using the correlation as theoretically approximated by Foster [24]. Due to the measurement of a relative displacement between allowed and forbidden transitions, the requirement for an absolute wavelength calibration is reduced.

Apart from the energy levels of the electronic states resulting in shifting and splitting of the spectral line components, the optical transitions are characterised by polarisation. The polarisation of line emission and its orientation to the electric field depend on the change of the magnetic quantum number m as follows:

$$\Delta m = \begin{cases} 0 & \pi - \text{polarised}, \\ \pm 1 & \sigma - \text{polarised}. \end{cases} \tag{4}$$

In the case of π-polarisation, the emission is linearly polarised and oriented parallel to the electric field direction. For σ-polarisation, the emission is circular polarised and oriented perpendicular to the electric field. The algebraic sign stands for the rotational direction of the circular polarised light. If the change is positive the rotational direction is clockwise, otherwise counterclockwise.

Since selection rule 2 regarding Δm applies in presence of electric fields for allowed as well as for forbidden transitions, several optical sub-transitions can occur for both components. Figure 1 shows exemplary all possible sub-transitions of the allowed 492.19 nm and forbidden 492.06 nm transition depending on upper magnetic quantum number m_u and lower magnetic quantum number m_l. In sum, there are nine possibilities for allowed and nine for forbidden transitions. Since in the electric field the degeneracy is not resolved with respect to m, the sign can be neglected (marked in grey) and just five transitions remain. Moreover, the sub-levels of the lower state ($n_l = 2$) are less influenced by electric fields and therefore m_l can be neglected and the observed changes are mostly dominated by m_u. Table 1 gives a summary of all possible transitions between m_l and m_u in form of $[m_u – m_l]^{\pi,\sigma}$ and the corresponding polarisation state for the allowed and forbidden sub-line.

The theoretically calculated correlation between wavelength displacements of these sub-transitions as shown in table 1 and electric field is illustrated in figure 2. Here, the reference point is the position of the unaffected allowed 492.19 nm line to which all displacements relate in this work. Three groups of very similarly behaving sub-transitions are indicated by straight lines.

Usually, a linear polariser is used (placed in between discharge sources and spectrometer) to further reduce the amount of involved lines [7, 20, 21, 23]. This polariser allows to suppress σ-polarisation resulting in a simpler emission spectrum and simpler analysis, consequently.

However, a polariser has no impact on the emission structure in the case of the MGA. Neither its insertion into the optical path nor its relative orientation to the MCPA lead to any change in the emission structure (not shown here). This is due to the radially symmetric shape of the cavities and the resulting prevailing electric field vector configuration. This is an overlay of components oriented parallel and radial to the observation and surface normal of the MGA. Therefore, a fitting procedure to determine electric field strengths in MGA must consider all five allowed and forbidden transitions.

2.1. Line broadening

Since the displacements between allowed and forbidden transitions are in a range of a tenth of a nanometer, broadening effects cannot be neglected. However, as in a previous work dealing with electric field strengths in an atmospheric pressure operated plasma jet [20], many line broadening mechanisms do not play a significant role under operation conditions used here. The estimated full width at half maximum (FWHM) of the Doppler ($\sim 10^{-3}$ nm), pressure ($\sim 10^{-3}$nm), natural ($\sim 10^{-6}$nm) Van der Waals ($\sim 10^{-3}$nm) and the Stark broadening ($\sim 10^{-7}$nm) provide negligible values.

In contrast to that, resonance broadening must be considered. The corresponding Lorentzian contribution to the FWHM can be calculated with equation (5) [28, 29].

$$f_{\mathcal{L}} = \Delta\lambda_{\text{Res}} = 1.63 \times 10^{-15} \sqrt{\frac{g_l}{g_u}} \lambda_0^2 \lambda_R f_R n_g. \tag{5}$$

It depends for the He I 492.19 nm transition on the statistical weights of upper $g_u = 5$ and lower $g_l = 3$ level. The atomic absorption oscillator strength $f_r = 0.273$ of the resonance transition wavelength is $\lambda_R = 58.4$ nm [30]. The particle density

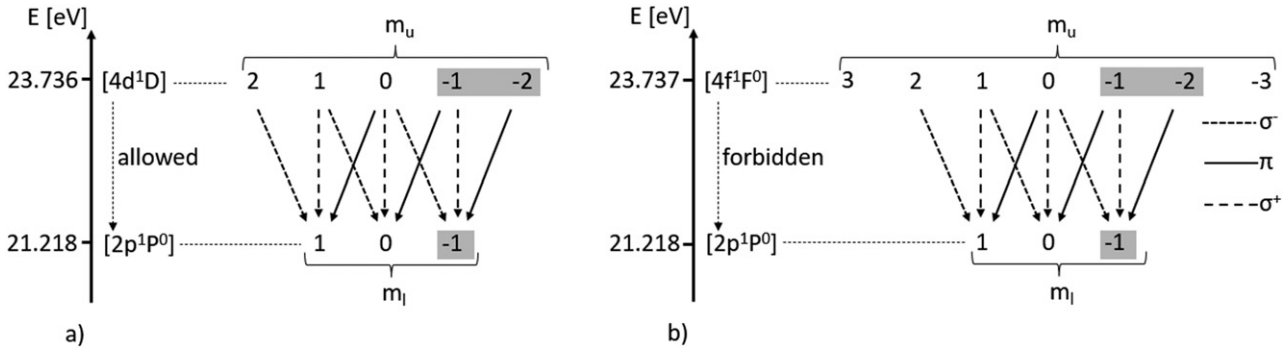

Figure 1. Schematic sketch of possible (a) allowed and (b) forbidden transitions depending on magnetic quantum number.

Table 1. Summary of all possible allowed and forbidden transitions and corresponding polarisation states depending on upper magnetic quantum number.

m_u	Transition
2	$[2\text{-}1]^{\sigma}$
1	$[1\text{-}1]^{\pi}$, $[1\text{-}0]^{\sigma}$
0	$[0\text{-}0]^{\pi}$, $[0\text{-}1]^{\sigma}$

n_g can be expressed in dependence on gas temperature T_g and pressure p by using the ideal gas law. In this study, the plasma source is operated at atmospheric pressure. The gas temperature is estimated to be 360 K obtained in a similar device by analysing the line width of a resonance broadened helium transition including a Van der Waals contribution [31]. This yields to a FWHM of $f_{\mathcal{L}} \approx 0.10$ nm being a factor of about 100 larger than the negligible Doppler broadening.

The contribution of the instrumental broadening $\Delta\lambda_{\text{Instr}}$ as the second not-negligible effect was measured by coupling 632.8 nm HeNe laser radiation in the optical setup. The broadening could be fitted with a Gaussian profile $\mathcal{G}$ having a FWHM of about $f_{\mathcal{G}} \approx 0.02$ nm.

3. Experimental

3.1. Metal grid array reactor

In figure 3 a schematic sketch of the used MGA reactor is depicted. This device can be divided into three main parts: an aluminium mounting, a carrier made from polyether ether ketone (PEEK) and a glass cover.

The carrier serves as a holder for the MGA. A 5 mm thick samarium–cobalt (Sm_2Co_{17}) magnet, having a length of 50 mm and a width of 15 mm, is inserted flush with the surface of the carrier and works as an electrically grounded electrode. However, the resulting magnetic field having a strength of about 0.2 mT is not strong enough to influence the discharge [13].

Additionally, magnetic fields can also cause a Zeeman pattern of optical lines. However, this should play no significant role here. In high power magnetron sputtering discharges (HIPMS) where clearly higher magnetic field strengths (up to 180 mT) occurs, Zeeman pattern was estimated to be still negligible [32]. Thus, under the assumption of almost similar Landé-g factor, Zeeman pattern is also negligible here.

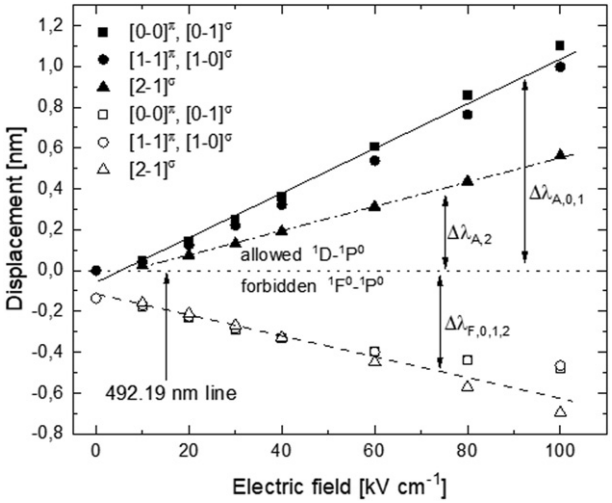

Figure 2. Displacements for allowed and forbidden transitions depending on the electric field, based on the calculation of Foster [24]. The reference value (dotted line) is the position of the unaffected allowed line.

A 88 mm long and 27 mm wide zirconium oxide foil (ZrO_2, relative permittivity $\epsilon_r \approx 27$) with a thickness of 40 μm covers the magnet and acts as a dielectric barrier between the magnet and a high-voltage (HV) supplied nickel foil on the top. Due to the magnetic character of the nickel foil, this three-layer structure (magnet, dielectric, nickel foil) is held together. The basic properties and comparability to other microplasma array concepts were shown and discussed in [13].

The nickel foil has the same dimensions as the dielectric with the exception of the thickness of about 50 μm. This MGA reactor is a modification of a single MGA [13] and consists of four so-called sub-arrays arranged in a row along the length of the nickel foil. A sketch of this foil is illustrated in figure 4. Each sub-array is separated from the adjacent by a distance of 1 mm (δs in figure 4) and covers a square with a base length of 10 mm. In every sub-array, laser-cut circular cavities of equal diameters are arranged in lines and columns. The distance between lines and columns is kept constant at 100 μm ((a) in figure 4). For cavities of 200 μm, 150 μm, 100 μm and

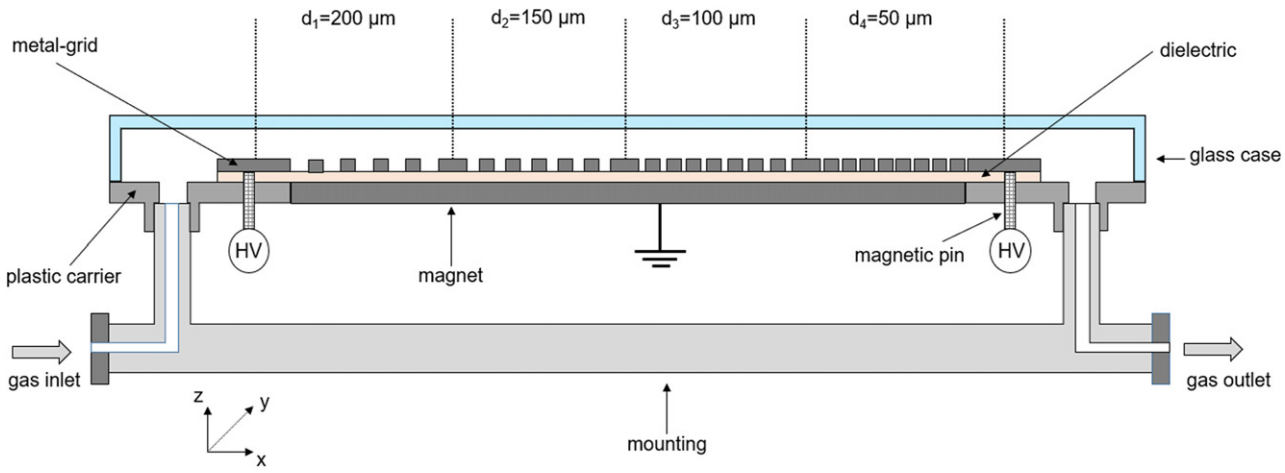

Figure 3. Schematic sketch of the MGA setup and the diagnostic system.

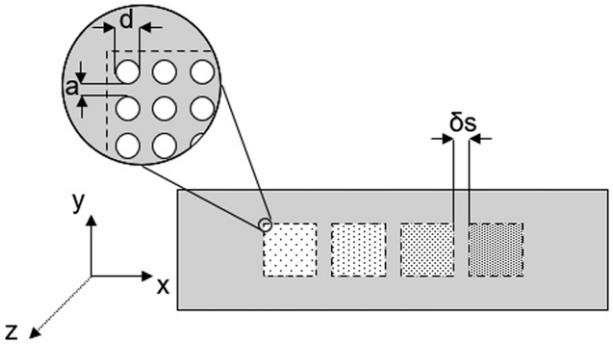

Figure 4. Schematic sketch of the nickel foil containing four different sub-arrays.

50 μm diameter ((d) in figure 4), this results in 26, 32, 48 and 56 cavities per line and column, respectively.

Due to that construction, all four sub-arrays are operated with identical electrical excitation, gas composition and material properties. This allows a more defined investigation and comparability of geometric influence of the cavities on the discharge than for individually installed and investigated (sub-)arrays.

At the bottom, the carrier is connected to the aluminium mounting, that enables gas supply via an adapter (Swagelok) and mounting to *xyz* stage (Zaber Technologies LSM100A-SV1). A mass flow controller (MFC, Analyt 2000 Series) ensures a controlled gas flow. In this paper, helium 5.0 (purity 99.999%) is used with a flow of 2 slm.

Finally, the upper side of the carrier is tightened with a glass cover (BK7). This allows optical access from the top and from the side for optical diagnostics and a sealed gas flow along the sub-arrays. To select emission of only one sub-array for optical investigations, an aperture whose opening has the same dimension as a single cavity structure can be positioned along the glass cover. The used optical diagnostics are described in the following sub-section.

3.2. Setup and diagnostic system

Figure 5 illustrates the experimental setup and the diagnostic system. The voltage supply is provided by a function generator (Tektronix AFG 3021B) connected to an amplifier (HV, FM Electronic DCU 600-40 HF). The temporal evolution of current and voltage are measured using a capacitive voltage probe (U-probe, Tektronix P6015A) and an inductive current probe (I-probe, Tektronix P6021) connected to an oscilloscope (Lecroy 8404M-MS, 4GHz bandwidth).

Optical emission spectroscopy (OES) is the main diagnostic tool in this paper and realised by a two m focal length plane grating spectrometer (PGS, Carl Zeiss Jena PGS 2) working with a 1302 mm^{-1} diffraction grating. The light is dispersed by the PGS and afterwards detected by a cooled ICCD-camera (Andor DH320T-25U-A3) having 1024 $\times$ 256 detector pixels with a size of 26 μm in imaging mode. This yields a pixel to pixel resolution of 8 pm in the first spectral order. The entrance slit is set to 20 μm. As mentioned before, the final instrumental profile was determined to be 0.02 nm. The position of the *field-free* (ff) line is verified by a reference measurement of a low power rf-driven atmospheric pressure microplasma jet operated in Helium. For phase-resolved investigations, the integrated delay unit of the ICCD-camera is triggered by the function generator.

A fibre-collimator combination captures and transfers the emission of a single sub-array to the entrance slit of the PGS. The fibre (Ocean Optics) has a diameter of 800 μm. To select the emission of a specific sub-array, this fibre-collimator combination can be positioned with an electrically driven stage.

A second fibre-collimator combination is used to monitor the time-resolved but wavelength integrated emission of a sub-array. The emission is transferred to a photomultiplier tube (PMT, Hamamatsu R3896).

In the following, a distinction of emission between two half-phases is made: (i) the increasing potential phase (IPP, $dU/dt > 0$) and (ii) the decreasing potential phase (DPP, $dU/dt < 0$).

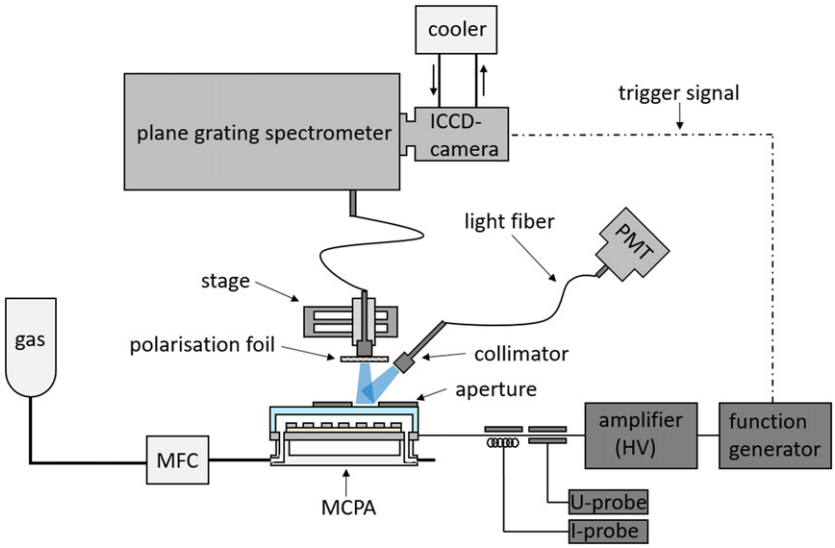

Figure 5. Synoptic of used setup and diagnostic system.

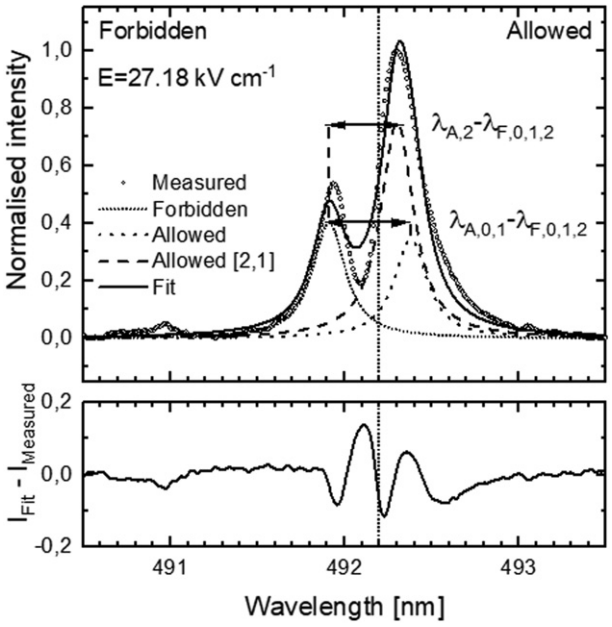

Figure 6. Measured (circles) and fitted (solid line) spectrum with all individual components. The composition contains the F, 0, 1, 2 group (short dotted), the A, 0, 1 group (dotted line) and the A, 2 group (dashed line). The spectrum was measured on the 200 μm cavities with a voltage amplitude of 600 V at a frequency of 15 kHz.

3.3. Fitting procedure

The upper part of figure 6 shows a measured spectrum (circles) of an MGA with 200 μm cavities integrated over the full IPP at an applied voltage of 600 V.

The spectrum shows a detailed structure due to the overlay of the various shifted and splitted sub-transitions. A fitting procedure was applied to deconvolute all sub-transitions in a measured emission spectrum. In this way, all relative displacements to the unaffected 492.19 nm line are obtained and can afterwards be calculated into electric field strengths. The resulting fitted spectrum (solid) and its individual components (short dotted, dotted, dashed) from the procedure below are also shown in the upper part of figure 6.

The final fit function is given by

$$\begin{aligned}\mathcal{F}(\lambda) = {} & \mathcal{V}_1(\alpha, A_1, \lambda, \lambda_1, \sigma) + \mathcal{V}_2(\alpha, A_2, \lambda, \lambda_2, \sigma) \\ & + \mathcal{V}_3(\alpha, A_3, \lambda, f(\lambda_1, \lambda_2), \sigma) \\ & + \mathcal{V}_{\mathrm{ff}}(\alpha, A_{\mathrm{ff}}, \lambda, 492.19\,\mathrm{nm}, \sigma)\end{aligned} \tag{6}$$

and depends on a superposition of four individual pseudo-Voigts profiles described by

$$\mathcal{V}(\lambda) = \mu \cdot \mathcal{L}(\lambda, A, w, \lambda_0) + (1-\mu) \cdot \mathcal{G}(\lambda, A, w, \lambda_0). \tag{7}$$

Pseudo-Voigt profiles were chosen due to the dominant Gaussian and Lorentzian broadening effects. Each one depends on the intensity amplitude A, the central wavelength λ_0 and standard deviation σ. Here, the standard deviation w is directly connected to the FWHM $f_{\mathcal{V}}$ with $2\sigma = f_{\mathcal{V}}$.

The final fitting equation (6) is based on the following assumptions and simplifications:

(I) As visible in figure 2, three groups of transitions can be identified that behave similarly. The transitions of each group are fitted by a simple single profile to reduce the total amount of lines from 10 to 3. The first group (F, 0, 1, 2, dashed line) comprises all forbidden transitions that shift almost identically with increasing electric field up to a value of about 70 kV cm^{-1}. The respective trend of the second group (A, 0, 1, full line) is describing all allowed transitions with $m_{\mathrm{u}} = 0, 1$ which almost overlap with each other over the whole displayed electric field range. For this reason, the mean value of both displacements with respect to the 492.19 nm transition was taken in previous works and is also used here. Its displacement (mean value) with respect to that of the forbidden lines is indicated as $\Delta\lambda_1 = \Delta\lambda_{A,0,1} + \Delta\lambda_{F,0,1,2}$. The indices mark the involved allowed (A) or forbidden (F) transitions with upper magnetic states. The third approximated group (A, 2, dashed dotted line) describes the allowed [2-1]

Table 2. Coefficients for equations (8) and (9).

i	a_i	b_i
0	(0.127 ± 0.004) nm	(2.307 ± 0.057) kV cm^{-1}
1	(0.258 ± 0.006) nm nm^{-1}	(33.028 ± 0.859) kV cm^{-1} nm^{-1}
2	(1.906 ± 0.066) nm nm^{-2}	(93.965 ± 2.631) kV cm^{-1} nm^{-2}
3	(-0.861 ± 0.031) nm nm^{-3}	(-40.356 ± 0.928) kV cm^{-1} nm^{-3}

transition. Its displacement to the first group is described by $\Delta\lambda_2 = \Delta\lambda_{A,2} + \Delta\lambda_{F,0,1,2}$.

(II) Assuming that the shifts are enforced by a single electric field, they have to be connected with each other by

$$\Delta\lambda_2 = a_3 \cdot \Delta\lambda_1^3 + a_2 \cdot \Delta\lambda_1^2 + a_1 \cdot \Delta\lambda_1 + a_0. \quad (8)$$

The coefficients for this and the following equations are listed in table 2.

(III) The corresponding electric field is calculated from the displacement $\Delta\lambda_1 = \Delta\lambda_{A,0,1} + \Delta\lambda_{F,0,1,2}$. The correlation is approximated by the third order polynomial function

$$E(\Delta\lambda_1) = b_3 \cdot \Delta\lambda_1^3 + b_2 \cdot \Delta\lambda_1^2 + b_1 \cdot \Delta\lambda_1 + b_0. \quad (9)$$

(IV) Due to the configuration of the MGA, the discharge can occur in areas of the cavity in particular outside in IPP as observed in [25] and figure 13(a) where the applied electric field is generally not strong enough or shielded too much for Stark shifting and splitting. This can result in the appearance of the unaffected so-called ff 492.19 nm line in the spatially-integrated spectrum. Consequently, the fitting procedure must consider this optical line in equation (6).

(V) Since all transitions only shift by a few tenths of a nanometer with respect to the ff transition, the broadening does not change significantly. Therefore, all transitions are described with identical standard deviation $w_i = w$ and ratio between Lorentzian and Gaussian $\mu_i = \mu$.

Here, the actual FWHM $f_\mathcal{V}$ is calculated to be 0.10 nm.

The exemplary fitted spectrum (figure 6) is composed of the three combined lines as described before. The ff component (short dashed) is not detectable in this fit due to its small intensity. This can be understood by comparison to calculated field strengths within a discharge channel of symmetric geometry [33]. Based on this, it is known that the electric field strengths are everywhere higher than 15 kV cm^{-1} and the ff emission can only occur from a discharge on the top of the nickel electrode. As a consequence, the field free component cannot be detected and the complete fit-procedure could have also been performed without the ff component. A significant difference in electric field strengths between both fit procedures is not detectable.

In general, the measured spectrum is described very well by this fitting-procedure. However, there are some small deviations as illustrated at the bottom part of figure 6. At the dip and on the right wing, the fit does not ideally match the measured spectrum. The main impact is the spatial integration within a single cavity. Thus, the measured spectrum is a result of contributions induced by various electric field strengths that cannot be considered ideally with a single electric field in the fitting procedure.

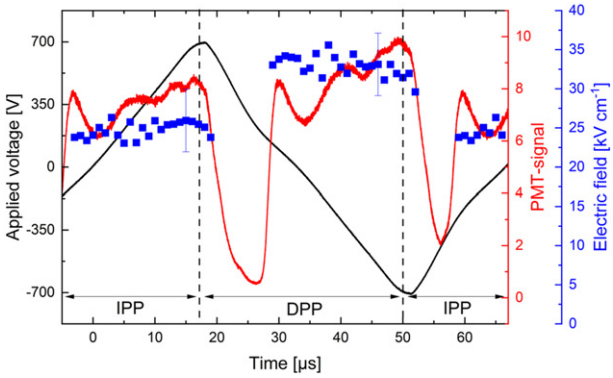

Figure 7. Time-resolved electric fields (blue squares) and cavity-integrated emission (red line) depending on triangular voltage excitation (black line) having a voltage amplitude at 700 V and a frequency of 15 kHz at a He flow of 2 slm at ambient pressure. The electric field measurement is done with a time-resolution of 1 μs. The cavities have a diameter of 200 μm.

A further factor is the half-phased time integration and the respective change with applied voltage. Its influence is described in section 4.1.

4. Results

4.1. Time-resolved measurements

To investigate the dynamics of electric field strengths depending on the bipolar triangular voltage excitation, time-resolved measurements are executed with a time-resolution of 1 μs. The time resolution is constrained by the weak emission of the dispersed line, the sensitivity of the detecting system and the resulting total measuring time. Figure 7 shows time-resolved electric field strengths (blue squares) calculated from measured spectra of 200 μm cavities depending on the excitation voltage (black line) a frequency of 15 kHz. To get a higher signal-to-noise ratio for this time-resolution, the voltage amplitude is set to be 700 V. To limit the power load on the devices for the upcoming half-phase resolved measurements, the voltage is reduced by 100 V. Additionally, the temporal evolution of the integral emission (thick red line) recorded with the PMT is displayed. A slight deviation from an ideal triangular excitation waveform is caused by the limited frequency response of the voltage amplifier (100 kHz).

For the selected operation conditions of 2 slm gas flow at atmospheric pressure, the spatially-integrated emission shows a comparatively smooth behaviour in IPP and DPP illustrated exemplary by black arrows in figure 7. After a peak following ignition, the intensity slowly rises for about 15 μs until the reversal of the voltage slope. The intensity in the DPP is about 20% higher and starts about 5 μs later than in the IPP. This is a deviation from the behaviour at lower pressures where several large intensity peaks could be observed [13]. These could be associated with ionisation waves travelling across the array. Here, a spatially homogeneous quasi-simultaneous ignition of all cavities is observed with phase resolved imaging using a

ICCD camera setup (not shown). Probably due to this spatial overlay of the numerous cavities, no individual emission pulses can be observed although the response time of the PMT circuit (about 5 ns) would allow this. So it is not possible to detect individual streamer occurrences.

In general, the measured electric field strengths are in a range of about 25 kV cm^{-1} and show a very good agreement with simulations done for similar devices such as SBA [34], pores [10] and discharge channels [33].

As a second observation, the electric field strengths are found to be higher in DPP than in the IPP by about 8 kV cm^{-1}. During the IPP the electric field strengths stay rather constant in a range between 20 and 22 kV cm^{-1}. A more explicit behaviour takes place in the DPP where the electric field strength slowly decreases by about 5 kV cm^{-1} with increasing applied absolute potential. This has to be compared to an error of about 4 kV cm^{-1} from the fitting routine and a statistical error of about 3.5 kV cm^{-1} comparing different data sets. Since these errors do not change significantly and for a better readability, only one error bar is shown per curve and per half-phase in graphs showing measured electric fields.

These observations can be understood in a simple picture based on the MGA configuration and time-dependent charge distribution effects. Furthermore it has to be kept in mind that the investigated emission is spatially integrated and based on excitation by accelerated electrons.

Firstly, the basically constant electric field strength agrees very well with the picture of a DBD streamer discharge where a streamer is suppressed when the generated space charge gets too large, but is reignited due to increasing external field and e.g. movement of ions. As a result, the local field strength overcomes again the ignition threshold [9]. Due to this continuous resetting of the local electric field in the individual cavities, only a certain constant average field can be established. This is further smoothed out by the overlay of contributions from the numerous cavities.

Secondly, the structure of MGA and the bipolar excitation lead to an asymmetric discharge characteristic [13]. In this asymmetry, electrons are accelerated into the direction of the dielectric i.e. into the cavity and it can be assumed that they cause emission in a high electric field regime during the DPP. During the opposite phase (IPP) the excitation takes place in lower occurring electric fields when the electrons move in opposite direction towards the cavity opening in the nickel electrode. This is sketched in figure 8.

At last, electrons cannot disappear from the dielectric after finishing their movement during the DPP and a charge distribution is built up in time. This charge density might then increase during time-dependent discharge excitation and causes a shielding of the fields so that the measured electric field decreases slowly in time, consequently. Since the nickel electrode is not covered by a dielectric, the electrons are lost there during the IPP and no charge distribution can be generated there. Hence, the electric fields stay more constant in this phase.

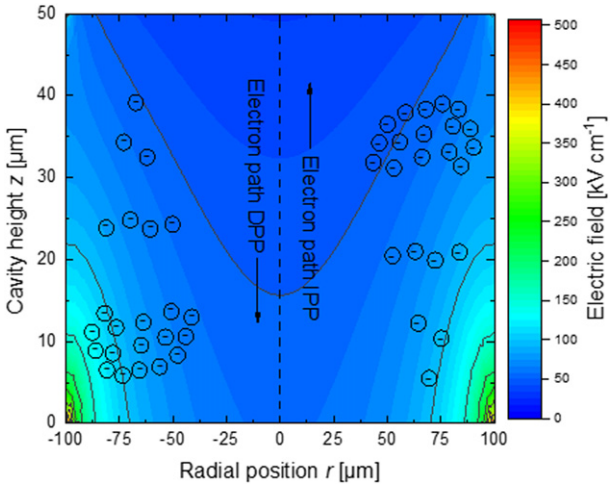

Figure 8. Computed applied electric field contribution within a 200 μm cavity under an applied voltage at 600 V. The dielectric surface is located at $z = 0$. The left side of this map illustrates the electron movement and multiplication during the DPP while the right side shows this procedure in IPP.

4.2. Parameter variation

It was shown with 1 μs time resolution that the observed average electric fields stay reasonably constant in both phases, further investigations were carried out half-phase resolved. To investigate how the electric field strengths within the cavities can be controlled, a series of accessible operation parameter variations were applied. Apart from geometric variations of the cavity, also the influence of excitation frequency, applied voltage amplitude and pressure was investigated.

4.2.1. Cavity diameter. A specific characteristic of micro plasma array discharges is the geometry and in this case the diameter of the cavities. It has been shown that this can significantly influence the behaviour of the arrays [11]. Figure 9(a) shows measured (symbols with dotted line) and modeled (broken lines without symbols, discussed in subsection 4.3) field strengths as a function of the cavity diameter. The MGA with its set of four sub-arrays with diameters ranging from 50 to 200 μm is operated with a voltage amplitude of 600 V and a frequency of 15 kHz. Due to some residual impurities (dust) and the small intensity of the used helium transitions, the emission signal is noisy for 50 μm cavities and the corresponding spectra cannot be fitted.

As expected, the electric field decreases with higher cavity diameters in both phases. This agrees with calculations for pores [10]. During DPP (red triangles), a decrease from about 65 kV cm^{-1} to 35 kV cm^{-1} occurs. A weaker effect is observed in IPP (black squares), where the electric field decreases from just about 35 kV cm^{-1} to 30 kV cm^{-1}. As for the time-resolved measurements, the electric field is higher in DPP than in IPP. This is also visible in all following parameter variations. In addition, it is noticeable that both field strengths approach each other with larger cavity diameters.

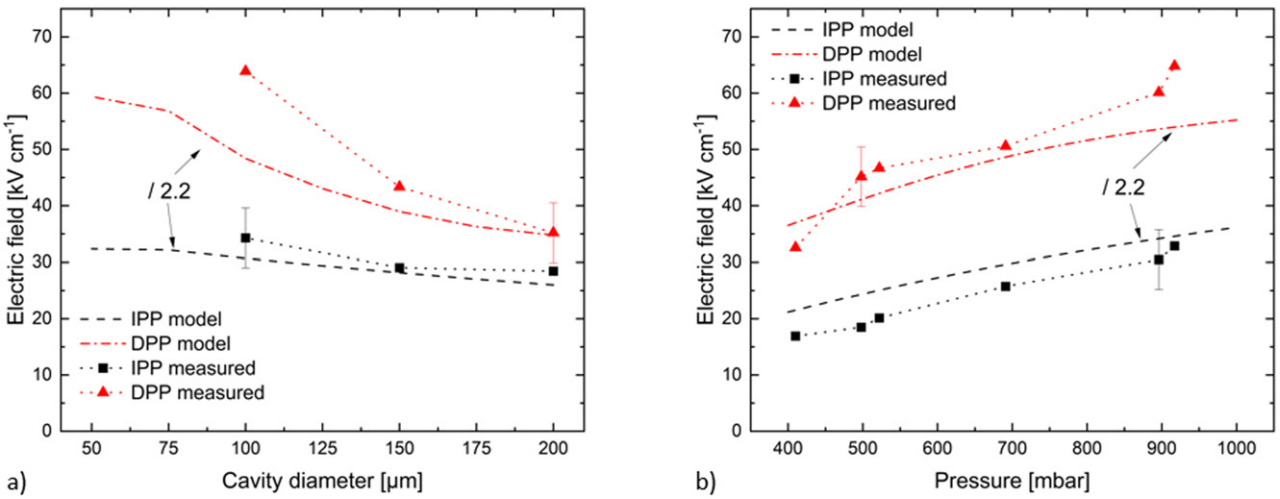

Figure 9. Measured and calculated electric field strengths as a function of (a) cavity diameter and (b) pressure during IPP (experiment: black squares; model: black dashed lines) and DPP (experiment: red triangles; model: red dotted dashed lines). In (a) the MGA is operated at atmospheric pressure and an excitation having a voltage amplitude at 600 V and frequency at 15 kHz. In (b) a single MGA having cavity diameters of 100 μm is operated with a voltage of 600 V and frequency at 15 kHz. In both cases the integration time is about 15 min.

Due to the asymmetric discharge geometry and the distribution of the applied electric field within the cavities, the measured trends can be understood. It is known from a similar geometric channel discharge [33] that the electric field has its greatest strength and the steepest increase at the boundary edge between the nickel foil and the dielectric. With this and the directional argument for the propagation of the electrons, these cause a discharge in the DPP in a higher electric field regime than during the IPP. Smaller cavity dimensions lead to a decreasing distance between the high electric field regions resulting in an averaged higher electric field in the complete cavity structure. Since the discharge is located closer to the dielectric during DPP where the field gradients are steepest, the increase of the electric field is more sensitive in this half-phase and also shows a stronger dependency on the cavity dimension than during the IPP.

4.2.2. Pressure. A further parameter for controlling the discharge within a microplasma array is given by pressure. To investigate its influence a device was installed in a vacuum chamber described previously [13]. Here, a single MGA having 100 μm cavities is operated with a voltage at 600 V and a frequency of 15 kHz.

Figure 9(b) shows that the measured electric field strengths increase with rising pressure for both half-phases. The corresponding modeled electric field strengths (broken lines without symbols) are discussed in section 4.3. During the IPP an increase from about 15 kV cm^{-1} to about 30 kV cm^{-1} is detectable. A nearly similar rising occurs in DPP where electric field strengths up to 65 kV cm^{-1} are reached. With respect to the reduced electric field (E/N, not shown here) an almost constant trend is obtained at about 350 Td during DPP and 150 Td during IPP.

The mean free path of electrons may be a main factor for this behaviour. The mean free path becomes shorter with higher pressures and the discharge can only ignite in higher electric field regimes. This agrees with measurements that were carried out on silicon-based devices [25]. It could be found that the discharge changes its shape within the cavity and shifts more and more to the cavity edge (high electric field region) with rising pressure.

Variations of pressure strongly influence the behaviour of the discharge. In the case of the microplasma arrays this may result in appearance of propagating ionisation waves connected with pulsing emission or a more diffuse appearance and a quasi-continuous emission. More detailed investigations would require further phase-resolved measurements.

4.2.3. Voltage. A parameter that is directly connected to the electric field strengths within cavities is the applied voltage amplitude. Here, it is varied between 400 V and 800 V for 200 μm and 100 μm cavities applied with frequency of 15 kHz at atmospheric pressure.

Figure 10 shows these electric field strengths for (a) 200 μm and (b) 100 μm wide cavities during IPP and DPP. As can be seen in figure 10(a) a strong dependency is not observable. While electric field strengths slowly decrease from about 37 kV cm^{-1} to 34 kV cm^{-1} in DPP, in the opposite potential phase electric field strengths are almost constant at 27 kV cm^{-1} within the limits of the indicated errors. Since it is known from the cavity diameter variation shown in figure 9(a) that the deviation of the fields between IPP and DPP rises with smaller cavities, the same voltage variation is done for 100 μm cavities. As shown in figure 10(b) for this case clear decreasing trends can be observed for both phases. During DPP, the electric field drops by about 10 kV cm^{-1} from 70 kV cm^{-1} down to 60 kV cm^{-1}. In IPP, the electric field drops only by half from about 35 kV cm^{-1} to 30 kV cm^{-1}.

These decreasing trends are unexpected as one would rather presume that higher applied electric fields yield higher electric fields everywhere in the cavities as observed for simulated pore discharge [10]. However, they are in accordance with the physical picture as discussed for the time-resolved electric field strengths before in section 4.1.

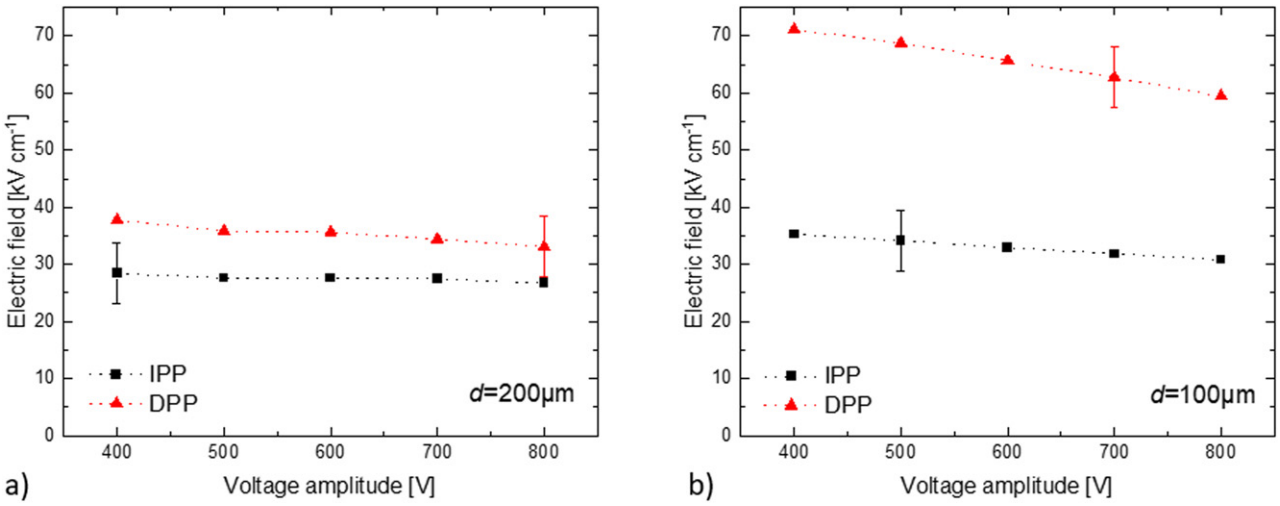

Figure 10. Electric field as a function of applied voltage during IPP and DPP for (a) 200 μm and (b) 100 μm cavities at atmospheric pressure. In both cases the applied frequency is set to be 15 kHz.

The higher applied voltage and coupled power into the discharge yields a rising ionisation rate and higher electron densities. Therefore, the absorption current onto the surface

$$j_{\mathrm{i(e)}}^{\mathrm{ads}} = n_{\mathrm{i(e)}} v_{\mathrm{i(e)}} \tag{10}$$

must increase where the absorption current $j_{\mathrm{i(e)}}^{\mathrm{ads}}$ depends on the the ion (i) or electron (e) density and their respective velocities $v_{\mathrm{i(e)}}$. In consequence, the surface charge distribution on the dielectric counteracting the applied electric field plays an increasing role.

The key role of these surface charges within discharge characteristic is already perceivable by taking into account the excitation indicated by the PMT-signal in figure 7. In both phases, the discharge already ignites before the zero-crossing of the applied voltage is reached. This has also been observed in micro-channel devices [33]. This effect gets stronger when increasing the voltage amplitude (not shown here). In IPP, the discharge ignites already at about -350 V that corresponds to 8 μs before zero-crossing of applied excitation. The surface charges generated in the previous half-phase support the necessary fields in the discharge gap and lower the ignition voltage. Conversely, this means that residual surface charges have counteracted the applied electric field in the half-phase before.

4.2.4. Frequency. To investigate how residual surface charges influence the discharge, the electric field is measured depending on the frequency changing the time between discharge operation in subsequent half-phases. Figure 11 shows electric field strengths in 200 μm cavities as a function of the applied frequency, varied between 5 kHz and 25 kHz while the applied voltage is kept constant at 600 V at atmospheric pressure.

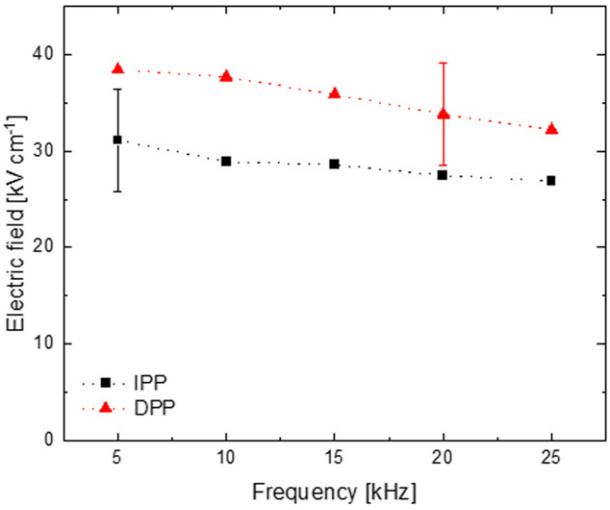

Figure 11. Measured electric field depending on applied frequency. The measurement is done at 200 μm cavities. The applied voltage is kept constant at 600 V.

It is illustrated that electric field strengths during IPP and DPP decrease with almost identical slope of about 6 kV cm^{-1} by increasing the applied frequency.

As in the case of the voltage variation, a higher electron density and shielding is also achieved due to the higher averaged coupled power by higher frequencies. Additionally, more surface and volume residuals remain after finishing a half-phase and promote the initial discharge conditions for the subsequent discharge. As an example, a greater initial electron density is available for the electron multiplication and shielding becomes more efficient. Since electrons cannot disappear after the DPP from the dielectric, they are available in a high amount for the

starting IPP. In case of the DPP the initial condition is enhanced by ions. During the IPP, they drift onto the dielectric and cannot contribute to an electron multiplication in the following DPP. However, they contribute to the gap voltage and support also an electron multiplication.

4.3. Basic model

To better understand the influence of the electron movement and its multiplication on the measured electric field strengths during both half-phases, a very simple and stationary Townsend model is set up. Therefore this model does not consider the temporal production of surface charges, but the spatial electron density in the cavity volume. For a first approach, only the cavity size and pressure variations are captured with this model. Additionally, this model takes into account that electric field strengths are obtained here by an OES-based technique. This means that the observed electric field is that experienced by the excited particles at the time of de-excitation by spontaneous emission. The correlation between the emissivity ϵ and the excited particle density n_{exc} is given by

$$\epsilon = \frac{hcA_{ik}n_{\mathrm{exc}}}{\lambda}, \tag{11}$$

where λ is the wavelength of emission and A_{ik} the Einstein coefficient for spontaneous emission. Assuming electron impact excitation, the task of this model is to correlate accelerating electrons within the applied electric field, the excited helium particle density and the density of electrons of sufficient energy to excite helium atoms.

The excited helium particle density n_{exc} is obtained here by a Corona model assuming that de-excitation is just taking place by spontaneous emission [35]. Since the discharge is operated with pure helium, quenching can be neglected in a first approach. The equation

$$\frac{\mathrm{d}n_{\mathrm{exc}}}{\mathrm{d}t} = n_{\mathrm{e}}n_{\mathrm{g}}X_{\mathrm{exc}} - A_{ik}n_{\mathrm{exc}} \tag{12}$$

describes this Corona model where n_{e} is the electron density, n_{g} the gas density and X_{exc} the excitation rate coefficient. The Einstein coefficient A_{ik} for the allowed 492.19 nm line is set to be $1.9863 \times 10^7\ \mathrm{s}^{-1}$ [36].

Since the dynamics of this discharge and time resolution of electric field measurement are in the microsecond range, these are by a factor of 100 slower than the lifetime of excited particles. Thus, it is sufficient to only consider a stationary density

$$n_{\mathrm{exc,\,sta}}(z) = \frac{n_{\mathrm{e}}(z)n_{\mathrm{g}}X_{\mathrm{exc}}(z)}{A_{ik}} = \frac{pn_{\mathrm{e}}(z)X_{\mathrm{exc}}(z)}{k_{\mathrm{B}}T_{\mathrm{g}}A_{ik}}. \tag{13}$$

By using the ideal gas law, the gas density can be substituted by pressure p and gas temperature T_{g}. Here, the gas temperature is estimated with 400 K [31].

The excitation rate coefficient is obtained by the following expression:

$$X_{\mathrm{exc}}(z) = \int_{E_{\mathrm{exc}}}^{\infty} \sigma_{\mathrm{exc}}(E)\sqrt{\frac{2E}{m_{\mathrm{e}}}}f(E)\mathrm{d}E. \tag{14}$$

Here, we assume a Maxwellian energy distribution $f(E)$ leading to an average electron energy $\tilde{E}$ and the energy dependent excitation cross-section σ_{exc} taken from [37]. The necessary excitation energy E_{exc} to excite from the ground state to the $[4d^1D]$-state is at 23.736 eV [36].

Since the average electron energy is almost unknown for such plasma sources, here we assume that this energy conforms with the energy $W(z)$ that electrons reach at some distance from the dielectric within their mean free path λ_{m} between collisions in presence of an applied electric field $E(z)$. That is described by

$$\tilde{E}(z) = W(z) = e\lambda_{\mathrm{m}}E(z). \tag{15}$$

The mean free path is calculated with

$$\lambda_{\mathrm{m}} = \frac{k_{\mathrm{B}}T_{\mathrm{g}}}{p\sigma_{\mathrm{cs}}}, \tag{16}$$

applying a total cross-section $\sigma_{\mathrm{cs}} = 4.6 \times 10^{-20}\ \mathrm{cm}^2$ [38].

The spatial electron density $n_{\mathrm{e}}(z)$ is estimated by using the following electron avalanche approach for the volume ionisation:

$$n_{\mathrm{e}}(z) = n_{\mathrm{e,0}}\ \exp(\alpha z)\,. \tag{17}$$

This electron multiplication depends on an initial electron density $n_{\mathrm{e,0}}$ and the volume ionisation length α. Since we assume a high number of residuals after each half-phase as discussed in the last sections, the initial electron density is estimated here with typical electron densities for DBD that are about $10^{12}\ \mathrm{cm}^{-3}$ [39].

With the assumed average electron energy $W(z)$ between subsequent collisions, the volume ionisation length can be estimated with a heuristic approach given by

$$\alpha(z) = \lambda_{\mathrm{m}}^{-1}\ \exp\left(\frac{-E_{\mathrm{ion}}}{W(z)}\right), \tag{18}$$

where E_{ion} stands for the ionisation energy. $E_{\mathrm{ion}} = 24.587$ eV in the case of helium.

Since ions have a much lower mobility than electrons, the dominant electric field E_{e} during electron avalanche is mainly given by the occurring electron density. Thus, the Poisson equation has the following form

$$\frac{\mathrm{d}E_{\mathrm{e}}}{\mathrm{d}z} = -\frac{e}{\epsilon_0}n_{\mathrm{e}}(z). \tag{19}$$

As a further simplification, we assume that the electrons are only accelerated in vertical z-direction in the cavity (z-direction in figures 3 and 4). This corresponds to the height in the cavity above the dielectric surface. Consequently, the electrons do not show a radial movement, here. To implement the asymmetric discharge characteristic we assume that electrons are accelerated from the dielectric ($z = 0\ \mu$m) to the cavity opening ($z = 50\ \mu$m) in the IPP. The opposite applies in DPP.

Under these assumptions and simplifications, we can calculate the electron density of sufficient energy at each height and radial position (r, z) within the cavity. These generate a number of excited helium atoms that subsequent decay with

the fluorescence at the shielded electric field $E_{\text{shield}}(z, r) = E(z, r) - E_{\text{e}}(z, r)$ at position (r, z).

Since measurements are executed spatially integrated, all calculated profiles ($E(z, r)$, $E_{\text{shield}}(z, r)$, $n_{\text{exc}}(z, r)$ and $n_{\text{e}}(z, r)$) have to be weighted with the cavity radius r before integration. For each component we apply

$$Y(z) = \frac{\sum_i Y(z, r_i) \cdot r_i}{\sum_i r_i}, \tag{20}$$

where $Y(z, r)$ stands for the respective profile.

The stationary electric field profile $E(z)$ is computed based on a COMSOL multiphysics 5.0 model for the geometric identical discharge channel [33]. It is illustrated as a map in figure 8. Since we neglect the time dependencies ($V(t) \rightarrow V$), the MGA is operated constantly with a voltage of 600 V.

5. Evaluation and comparison of modelled and measured electric field behaviour

Under consideration of these calculated profiles illustrated in figures 12(a) and (b) the difference between measured electric field strengths in IPP and DPP can be understood.

Based on the described model, figure 12 represents the calculated and normalised profiles of electron density (dotted line), excited helium particle density (dashed dotted line) and the shielded electric field (broken line) depending on the applied electric field profile (full line) in z-direction. $z = 0$ represents in both sub-figures the position of the dielectric surface. The arrows on the bottom of both sub-figures describe the direction of the movement of an electron. For the IPP case (figure 12(a)) at the beginning the electrons can absorb the required energy for ionisation, resulting in a rising electron density. Simultaneously, these electrons are able to excite helium atoms by electron impact excitation and therefore an excited particle density is also built up. Since the electric field decreases along the electron path, at some distance z sufficient energy for ionisation and excitation cannot be reached anymore and the production of further electrons and excited particles is reduced. Thus, the electron density slowly reaches a plateau and shielding does not become stronger. However, it has to be mentioned that for the calculation of this density electron losses caused by electron drift and recombination are not implemented in this simple model. Following the path due to the further reducing electron energy and finally stopped production, no further helium atoms are excited and de-excitation by spontaneous emission dominates. As a result, the excited particle profile has a peak-form structure with a maximum at $z = 12$ μm. Since the emissivity depends linearly on the excited particle density, the greatest contribution of the detected electric field comes from this region.

As can be seen in figure 12(b) describing the DPP, the electron and excited helium particle densities rise continuously as the electric field profile. Densities up to 10^{16} cm^{-3} (excited helium particles) and 8×10^{13} cm^{-3} (electron) at the surface are reached (correspond to the maximum in the normalised right axis). In this phase, the highest excited helium particle density is clearly located in the high electric field region close to the dielectric. Therefore, it becomes clear why higher electric fields are observed in the DPP in comparison to the IPP. While the maximum excited particle density is reached close to the dielectric in the regime of highest electric fields in the DPP, the maximum of excited species is generated a few micrometers away from dielectric in a rather lower electric field region during the IPP.

Due to the strong increase in the electron density in the DPP, the model shows that shielding of the electric field (dashed line) gets more effective and therefore the field finally drops. This supports the hypothesis of a building-up of charge density responsible for the slowly decreasing electric field in DPP for the time-resolved measurement shown in figure 7.

5.1. Effect of parameter variations

The basic Townsend model also allows some further insight into the experimental parameter variations.

5.1.1. Cavity diameter. Although this basic model does not directly consider the cavity diameter, a changing cavity dimension leads to a different electric field profile within the cavity. Thus, for each cavity diameter the applied electric field contribution is calculated using COMSOL and implemented in this model.

To compare the measured values with the model considerations, the line of sight character of the experiments has to be taken into account. Since the emission from excited particles occurs from all locations along the cavity height z, the calculated field strengths E_{cal} are obtained by averaging the shielded electric field E_{shield} with the excited helium particle density n_{exc} described by the following equation

$$E_{\text{cal}} = \frac{\sum_i E_{\text{shield}}(z_i) \cdot n_{\text{exc}}(z_i)}{\sum_i n_{\text{exc}}(z_i)}. \tag{21}$$

As visible in figure 9(a) the basic model (dashed dotted and broken lines) reproduces the measured electric field trends for the cavity variation for both phases quite well. However, the calculated electric field strengths are by a factor of about 2.2 higher. This can be attributed to the simplification that electrons are only accelerated in z-direction. Especially, close to the cavity edge characterised by high electric fields, the electron path may deviate significantly.

This electric field within the cavities has additional radial components at the cavity edge [33]. Thus, electrons do not move straight in z-direction but rather in a kind of concentric motion around the boundary edge between the dielectric and the nickel foil. Thus, the electron paths at high electric field regime are shortened and high electron and excited helium particle densities cannot establish in the high field regions. With this the contribution to the averaged measured field is reduced and the measured electric field strength decreases.

These radial contributions are stronger in smaller cavities. This may explain the increasing deviation between calculated and measured electric field strengths for smaller cavities.

An indication for the change from rather vertical to radial electric field components with smaller cavities can be found in

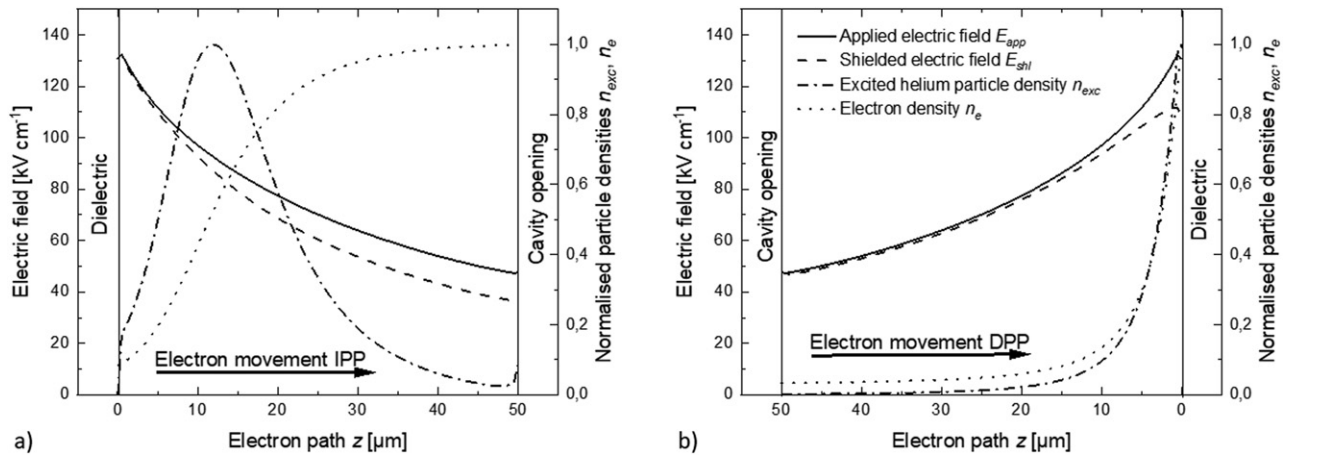

Figure 12. Weighted applied (full line) and shielded (broken line) electric field profile along the cavity height and corresponding normalised electron density (dotted line) and excited helium particle density (dashed dotted line) for (a) IPP and (b) DPP. The MGA is operated with a constant voltage of 600 V. The initial electron density is set to be 10^{12} cm^{-3}.

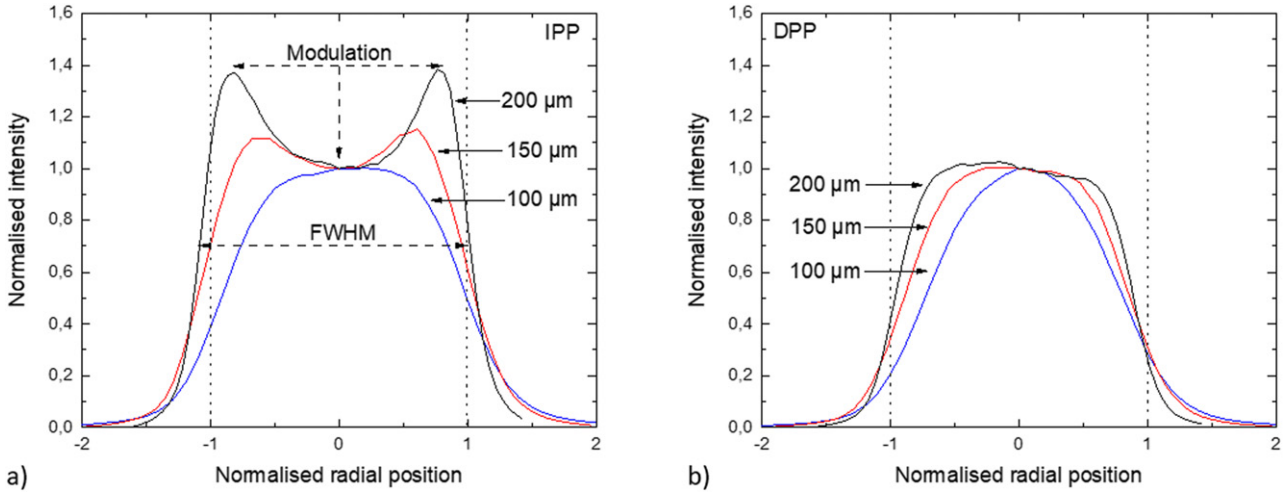

Figure 13. Radial 706 nm emission profile within various sized cavities during (a) IPP and (b) DPP. The applied excitation is adjusted at 600 V and 15 kHz.

the changing of the 706 nm helium emission profile with the cavity radius. Figure 13 shows this emission profile for various cavity diameters detected in a head-on observation during (a) IPP and (b) DPP. The intensity is normalised to the intensity at the centre of the cavity. The radial position is normalised by the cavity radius.

During DPP, the emission has a plateau-like shape in 200 μm cavities that disappears to the edges and gets sharper with smaller cavities. The stronger radial electric field pushes the discharge together. In IPP, a modulation is noticeable for larger cavity diameters. That means that an increasing emission occurs close to the cavity edges and drops in direction to the cavity centre. This modulation disappears and the FWHM of this profile decreases with decreasing cavity diameters. Finally at 100 μm, a structure is detected that is similar to the DPP. This fact can be understood from stronger radial electric field components, that accelerate electrons directly to the nickel electrode where they disappear. Thus, a shorter electron path for creating a significant high excited helium particle density is not available and the emission drops.

5.1.2. Pressure. The basic model also reproduces the trend of the pressure variation. This is shown in figure 9(b). A higher pressure yields a shift of the excited particle density maximum to the higher electric field regions. Due to more and more collisions the mean free path of the electrons decreases with higher pressure and thus increases the volume ionisation length as shown in equation (18). However, the decreasing electron energy lowers the ionisation probability term $\exp(-E_{\mathrm{ion}}/W(z))$ resulting in less ionisation and shielding, consequently.

Since the pressure typically influences the discharge operation significantly by an overlap of many processes this interpretation has to be taken with caution.

5.2. Frequency and voltage

As mentioned before, this model does not consider time-dependencies or surface charges. Thus the built-up of residuals that influence the following phase is out of the scope of this model. To get a first estimation which influence these surface charges might have on the voltage dependence, the dielectric is covered with a typical surface charge density between 10^{10} cm^{-2} and 10^{11} cm^{-2} [9] in the basic model. Such an increase of surface charge density could be induced by the increased ionisation with higher applied voltage. When the dielectric is covered with ions in IPP and with electrons in DPP, the calculated field decreases. That is in consistence with observations during voltage variation. The stronger dependence and difference between IPP and DPP in the smaller cavities might be explained by higher losses to the cavity walls.

6. Conclusion

This study focuses on the electric field strengths in a metal-grid array that is operated in pure helium and contains four sub-arrays consisting of micro cavities with varying diameters in the 100 μm range. Thus, all operating under the same conditions.

The interaction of field, electrons and species will determine the plasma-chemical processes for example for removal of volatile organic compounds or plasma catalysis.

To analyse the electric fields, the Stark shifting and splitting of a helium line pair could be successfully exploited in two different time-resolutions (1μs and half-phase). This approach provides reasonable values of about 40 kV cm^{-1} for the electric field that are in good agreement with similar plasma sources. Due to the emission spectroscopic nature of the diagnostics, the results are averaged over space but the region of maximum emission will also coincide with the region of maximum plasma chemical activity since here enough electrons of sufficient energy for processes such as dissociation are available.

A time-resolved investigation showed that a constant field strength is seen by the emitting helium atoms throughout the discharge operation. This supports the picture of a repetitively suppressing discharge by space charges and re-ignition by rising the applied external field.

With a half-phase time-resolution, the electric field could be investigated depending on geometric cavity dimensions and further excitation parameters. The field strengths are very well reproducible with each other from variation to variation.

The electric field strength can be controlled by the polarity of the applied excitation, resulting in higher strengths during the decreasing potential phase than in the increasing one. This can be influenced by the geometry/diameter of the individual cavities of the arrays. Additionally, the pressure turns out to be determining parameter allowing controllable electric field strengths within the cavities. This may allow a specific tuning of processes.

To better understand the physical excitation process, a simple stationary Townsend model was set up. This model supports the observed asymmetric discharge characteristic that can explain the distinction in electric field strengths between the increasing and decreasing potential phase. With the exception of the absolute values, the trends for the cavity and pressure variation can be reproduced.

To verify these measurements, a comparison using the 'electric field induced second harmonic' method with a higher spatial and temporal resolution is planned. For this the micro-channel variation of the MGA could be used which provides access from the side to the discharge volume. This would also give the chance to design a model that considers the spatial and temporal electron dynamics within the cavity.

Acknowledgments

This work has been supported by the German Research Foundation (DFG) within project A6 of the collaborative research centre SFB 1316 'Transient atmospheric plasmas — from plasmas to liquid to solid'. SI acknowledges the guest scientist Grant from the SFB 1316.

Data availability statement

The data that support the findings of this study are available upon reasonable request from the authors.

ORCID iDs

Sebastian Dzikowski https://orcid.org/0000-0001-5036-6770
David Steuer https://orcid.org/0000-0003-3005-0829
Sylvain Iséni https://orcid.org/0000-0002-4923-1657
Judith Golda https://orcid.org/0000-0003-2344-2146
Marc Böke https://orcid.org/0000-0003-1062-5808
Volker Schulz-von der Gathen https://orcid.org/0000-0002-7182-3253

References

[1] Becker K H, Schoenbach K H and Eden J G 2006 *J. Phys. D: Appl. Phys.* **39** R55–70
[2] Eden J G and Park S-J 2005 *Plasma Phys. Control. Fusion* **47** B83
[3] Koutsospyros A, Yin S-M, Christodoulatos C and Becker K 2004 *Int. J. Mass Spectrom.* **233** 305–15
[4] van Durme J, Dewulf J, Leys C and van Langenhove H 2008 *Appl. Catal.* B **78** 324–33
[5] Bogaerts A *et al* 2020 *J. Phys. D: Appl. Phys.* **53** 443001
[6] Whitehead J C 2016 *J. Phys. D: Appl. Phys.* **49** 243001
[7] Cvetanović N, Martinović M M, Obradović B M and Kuraica M M 2015 *J. Phys. D: Appl. Phys.* **48** 205201
[8] Starikovskaia S M, Allegraud K, Guaitella O and Rousseau A 2010 *J. Phys. D: Appl. Phys.* **43** 124007
[9] Golubovskii Y B, Maiorov V A, Behnke J and Behnke J F 2002 *J. Phys. D: Appl. Phys.* **35** 751–61

[10] Zhang Y-R, van Laer K, Neyts E C and Bogaerts A 2016 *Appl. Catal.* B **185** 56–67
[11] Kulsreshath M K, Golda J, Schulz-von der Gathen V and Dussart R 2014 *Plasma Sources Sci. Technol.* **23** 045012
[12] Eden J G *et al* 2003 *J. Phys. D: Appl. Phys.* **36** 2869–77
[13] Dzikowski S, Michaud R, Böttner H, Dussart R, Böke M and Schulz-von der Gathen V 2020 *Plasma Sources Sci. Technol.* **29** 035028
[14] Kozlov K V, Wagner H-E, Brandenburg R and Michel P 2001 *J. Phys. D: Appl. Phys.* **34** 3164
[15] Tanaka D, Matsuoka S, Kumada A and Hidaka K 2009 *J. Phys. D: Appl. Phys.* **42** 075204
[16] Gibalov V I and Pietsch G J 2000 *J. Phys. D: Appl. Phys.* **33** 2618
[17] Aljammal F, Gaborit G, Bernier M, Iseni S, Galtier L, Revillod G and Duvillaret L 2021 *IEEE Trans. Instrum. Meas.* **70** 1–9
[18] Goldberg B M, Shkurenkov I, Adamovich I V and Lempert W R 2016 *Plasma Sources Sci. Technol.* **25** 045008
[19] Bibinov N, Knake N, Bahre H, Awakowicz P and Schulz-von der Gathen V 2011 *J. Phys.D:Appl.Phys.* **44** 345204
[20] Hofmans M and Sobota A 2019 *J. Appl. Phys.* **125** 043303
[21] Kuraica M M and Konjević N 1997 *Appl. Phys. Lett.* **70** 1521–3
[22] Kuraica M M, Konjević N and Videnović I R 1997 *Spectrochim. Acta* B **52** 745–53
[23] Obradović B M, Ivković S S and Kuraica M M 2008 *Appl. Phys. Lett.* **92** 191501
[24] Foster J S 1927 *Proc. R. Soc. London* A **117** 137–63
[25] Kulsreshath M K, Golda J, Felix V, Schulz-von der Gathen V and Dussart R 2014 *J. Phys. D: Appl. Phys.* **47** 335202
[26] Langstroth G O 1930 *Proc. R. Soc. London* A **129** 70–91
[27] Obradović B M and Kuraica M M 2008 *Phys. Lett.* A **372** 137–40
[28] Konjević N 1999 *Phys. Rep.* **316** 339–401
[29] Ali A W and Griem H R 1965 *Phys. Rev.* **140** A1044
[30] Drake G 2006 High precision calculations for helium *Springer Handbook of Atomic, Molecular, and Optical Physics* ed G ed Drake (Berlin: Springer) pp 199–219
[31] Iseni S, Michaud R, Lefaucheux P, Sretenović G B, Schulz-von der Gathen V and Dussart R 2019 *Plasma Sources Sci. Technol.* **28** 065003
[32] Held J, Hecimovic A, von Keudell A and Schulz-von der Gathen V 2018 *Plasma Sources Sci. Technol.* **27** 105012
[33] Kreuznacht S, Böke M and Schulz-von der Gathen V 2021 *Plasma Sources Sci. Technol.* **30** 015014
[34] Kushner M J 2004 *J. Appl. Phys.* **95** 846–59
[35] Fantz U 2006 *Plasma Sources Sci. Technol.* **15** S137–47
[36] Kramida A and Ralchenko Yu (NIST ASD Team) 2021 NIST Atomic Spectra Database https://physics.nist.gov/asd
[37] Ralchenko Y, Janev R K, Kato T, Fursa D V, Bray I and de Heer F J 2008 *At. Data Nucl. Data Tables* **94** 603–22
[38] Pack J L, Voshall R E, Phelps A V and Kline L E 1992 *J. Appl. Phys.* **71** 5363–71
[39] Massines F, Gherardi N, Naudé N and Ségur P 2009 *Eur. Phys. J. Appl. Phys.* **47** 22805